Unveiling the Adsorption-Desorption Mechanism in Phosphorus-Doped Activated Carbon for Enhanced Double-Layer Pouch-Cell Supercapacitors

Jie Lei+,[a] Shenglong Li+,[a] Yanchen Liu,[a] Taoxiang Wang,[b] Jin Li,[a] Minghui Gu,[a] Hengjian Pu,[a] Kang Li,*[b] Teng Zhai,*[a] Hui Chen,[c] and Hui Xia[a]

Activated carbon (AC) suffers from low energy density in the organic system of electric double-layer capacitors (EDLCs). Currently, the research spotlight for enhancing the specific capacitance of AC in EDLC is to optimize the pore size distribution and enhance the specific surface area, but the increase of porosity in turn decreases the conductivity of AC. The surface modification is an effective strategy to improve the surface properties of carbon electrodes and enhance electrochemical performance. However, little attention has been paid to the interaction between AC surface and organic electrolyte. In this work, we have developed a phosphorus doping aimed at modulation of adsorption/desorption dynamics of organic electrolytes on the AC electrode. It was found that the phosphorus-carbon bonding increases the adsorbed amounts of TEA^+/BF_4^- per unit surface area, altering the charge storage mechanism and leading to improved specific capacitance. Furthermore, we fabricated a symmetrical pouch-cell supercapacitor with an energy density of 36.2 Wh kg^{-1}. The capacitance retention of 93.7% was maintained after 30,000 cycles at a current density of 10 A g^{-1}. These findings significantly advance our understanding of the charge storage dynamics in phosphorus-doped AC and will guide the design of improved carbon-based supercapacitors.

1. Introduction

The growing energy crisis has driven researchers to concentrate on exploring novel materials for the advancement of superior energy storage systems. Supercapacitors have attracted considerable interest due to their rapid charge/discharge capabilities and excellent cycling stability. However, the energy storage mechanism inherent to supercapacitors typically results in a lower energy density than that of batteries. Consequently, extensive research has been conducted on the types and modifications of electrode materials to mitigate this limitation. Activated carbon (AC) is widely utilized as an electrode material in commercial supercapacitors, owing to its unparalleled advantages such as high specific surface area, abundant porosity, low cost, and stable physicochemical properties. A variety of carbon precursors can be employed to synthesize activated carbon through templating and activation methods. For example, the large content of long-chain hydrocarbons and less volatile components in heavy oils can contribute to an optimal pore size distribution during the carbonization and activation processes.[1–3] However, excessively high porosity can lead to a decrease in AC conductivity. Achieving high rate and high energy density at the same time remains a great challenge for carbon-based supercapacitors, particularly in organic electrolytes.

The surface chemistry of carbon electrodes predominantly contribute to the electrochemical performance of EDLCs.[4] Phosphorus doping is a prevalent strategy to improve the properties of carbon electrodes in both the surface and bulk phases.[5,6] The introduction of heteroatoms can alter the electronic structure of carbon and provide additional active sites,[7] thus increasing the electronic conductivity and improving the specific capacitance of carbon materials.[8] The high electron donating property of phosphorus doping improves the charge transport and storage capabilities of carbon materials.[9] Zhong *et al.*[10] reported the synthesis of phosphorus-doped porous carbon nanosheets, which exhibited a high specific surface area of 2067.0 m^2 g^{-1}, a high capacity of 54.1 mAh g^{-1} at 5 A g^{-1}, and an excellent capacity retention of 86.8% after 9500 cycles at 1 A g^{-1}. Liu *et al.*[11] utilized chitosan as a nitrogen-riched carbon source and phytanic acid as a phosphorus source and activator to prepare self-embedded N,P-co-doped hard carbons, which exhibited a high discharge capacity of 105.6 mAh g^{-1} at 0.1 A g^{-1} and an excellent capacity retention of 89.3% after 4000 cycles. However, little attention has been concentrated on the interactions between the phosphorus-doped AC surface and organic electrolytes.

[a] J. Lei,+ S. Li,+ Y. Liu, J. Li, M. Gu, H. Pu, Prof. T. Zhai, Prof. H. Xia
School of Materials Science and Engineering, Nanjing University of Science and Technology, Nanjing 210094, China
E-mail: tengzhai@njust.edu.cn

[b] T. Wang, K. Li
Luoyang R & D Center of Technology of SINOPEC Engineering (Group) CO. Ltd., Luoyang, Henan 471003, China
E-mail: likang.segr@sinopec.com

[c] H. Chen
China Petroleum & Chemical Corporation, Beijing 100027, China

[+] These authors equally contribute to this work.

Supporting information for this article is available on the WWW under https://doi.org/10.1002/batt.202400730

Batteries & Supercaps

Research Article
doi.org/10.1002/batt.202400730

Chemistry Europe
European Chemical
Societies Publishing

In this study, we have successfully integrated phosphorus homogeneously into the surface of the carbon electrode. The phosphorus-carbon bonds are effectively grafted onto the carbon electrode, leading to a transformation in the charge storage mechanism and an augmentation in the number of adsorption sites. According to the electrochemical quartz crystal microbalance (EQCM) results, PAC-200 (where 200 denotes the phosphating temperature) exhibits a significantly enhanced adsorption, increasing from 1.41 μg to 5.48 μg, and the charge storage mechanism is primarily ion exchange at full potential. This leads to an elevated specific capacitance compared to untreated activated carbon (AC). Furthermore, we constructed a symmetrical pouch-cell supercapacitor with an energy density of 36.2 Wh kg^{-1} at a power density of 113.9 W kg^{-1}, which is notably sustained at 32.3 Wh kg^{-1} even at an elevated power density of 2272.8 W kg^{-1}. The device also demonstrates a remarkable capacitance retention of 93.7% after 30,000 cycles at a current density of 10 A g^{-1}.

Experimental Section

Synthesis of PAC-x (x Represents the Phosphating Temperature)

Phosphorization was conducted within a tube furnace under a slow flow of argon gas, utilizing NaH$_2$PO$_2$ as the upstream phosphorus source. The AC utilized in our study was obtained from SINOPEC ENGINEERING GROUP LUOYANG R&D CENTER OF TECHNOLOGY (SEGR-800, Luoyang, China). This particular AC was derived from heavy oil-based precursors including pitch and petroleum coke. The mass ratio of AC to NaH$_2$PO$_2$ was 3:8. The tube furnace was ramped up to 200/250/300/350 °C at a rate of 5 °C per min, and these temperatures were sustained for half an hour to obtain phosphorus doped PAC-x samples.

Material Characterization

The morphology of the material is observed using scanning electron microscopy (SEM, Quant 250FEG) and transmission electron microscopy (TEM, FEI Talos F200X G2). The crystal structure and defects of the prepared samples are characterized using X-ray diffractometer (XRD, Bruker D8) and Raman spectroscopy (Aramis, including in situ Raman measurements). Nitrogen adsorption-desorption isotherms are quantified with the ASAP 2460 porosimeter to determine the specific surface area (SSA) and pore size distribution (PSD) of AC and PAC-x. Elemental composition analysis is conducted using X-ray photoelectron spectroscopy (XPS, Thermo Scientific K-Alpha+).

Electrochemical Measurements

Carbon electrodes are fabricated from the prepared carbon materials (AC, PAC-200, PAC-250, PAC-300, PAC-350), comprising a mixture of 80% carbon, 10% Super-P, 10% Carboxymethyl cellulose sodium (CMC). This mixture is dissolved in minimal amount of deionized water and ground in a quartz mortar to form a homogeneous slurry over 20 minutes. The prepared slurry is then spread onto a carbon-coated aluminum foil current collector and subsequently dried in an oven at 80 °C for 8 hours. Symmetrical two-electrode supercapacitors (mass ratio of positive and negative electrodes=1:1) are assembled under an argon atmos-

phere. A 16 mm diameter glass fiber is employed as the separator, and 1 mol L^{-1} tetraethylammonium tetrafluoroborate (TEABF$_4$) in Ppropylene carbonate (PC) serves as the organic electrolyte within the CR2025 cell. The electrochemical performance is evaluated using a workstation that conducts cyclic voltammetry (CV, Corrtest CS350H) and galvanostatic charge-discharge (GCD, NEWARE BTS-610) in the electrochemical window of 0–2.5 V. Electrochemical impedance spectroscopy (EIS) is performed by applying a small sinusoidal amplitude of 10 mV in the frequency range from 0.01 Hz to 1,000,000 Hz.

The specific capacitance of the electrode is calculated based on the GCD curve with the formula:

$$C = 4\frac{I\Delta t}{m\Delta V} \ (\text{F g}^{-1}) \tag{1}$$

where I is the current density (A) and Δt is the discharge time (s), m is the mass of two single electrode and ΔV is the discharge potential window (V).

The formulas for energy density and power density are as follows:

$$E = \frac{1}{2} \times \frac{1}{4} \times \frac{1}{3.6}CV^2 \ (\text{Wh kg}^{-1}) \tag{2}$$

$$P = \frac{3600 \times E}{t} \ (\text{W kg}^{-1}) \tag{3}$$

t is the discharge time (s), V is the potential window during the test (V).

For the electrochemical quartz crystal microbalance measurements (EQCM, srsqcm-200), a slurry is prepared containing 7 mg of activated carbon (AC, PAC-200), and 2 mg of Super-P, and 1 mg of polyvinylidene fluoride (PVDF) dissolved in 500 μL of N-methylpyrrolidone (NMP). A few quantities of this slurry are then deposited onto a gold-plated quartz wafer (fundamental frequency 5 MHz). The carbon-coated gold-plated quartz wafer is dried overnight in an oven at 60 °C. The srsqcm-200 is combined with a Corrtest electrochemical workstation to perform concurrent EQCM and electrochemical measurements. The electrochemical setup employs a three-electrode system, utilizing the carbon-coated gold-plated quartz wafer as the working electrode, a platinum electrode as the counter electrode, and Ag/AgCl electrode as the reference electrode.

2. Results and Discussion

The morphological and microstructural characteristics of the samples were elucidated through scanning electron microscopy (SEM) and transmission electron microscopy (TEM). The SEM images of PAC-200 and AC samples, as depicted in Figure 1a, b, demonstrate that the irregular particulate morphology of the activated carbon remains unchanged following phosphorization. Multielement energy-dispersive X-ray spectroscopy (EDS) mapping images (Figure 1c) reveal the uniform distribution of phosphorus across the surface of the activated carbon. As clearly shown from the TEM images (Figure 1d–g), both AC and PAC-200 display the highly disordered and distorted lamellar structure of carbon, featured by an abundance of short-range carbon layers. Both PAC-200
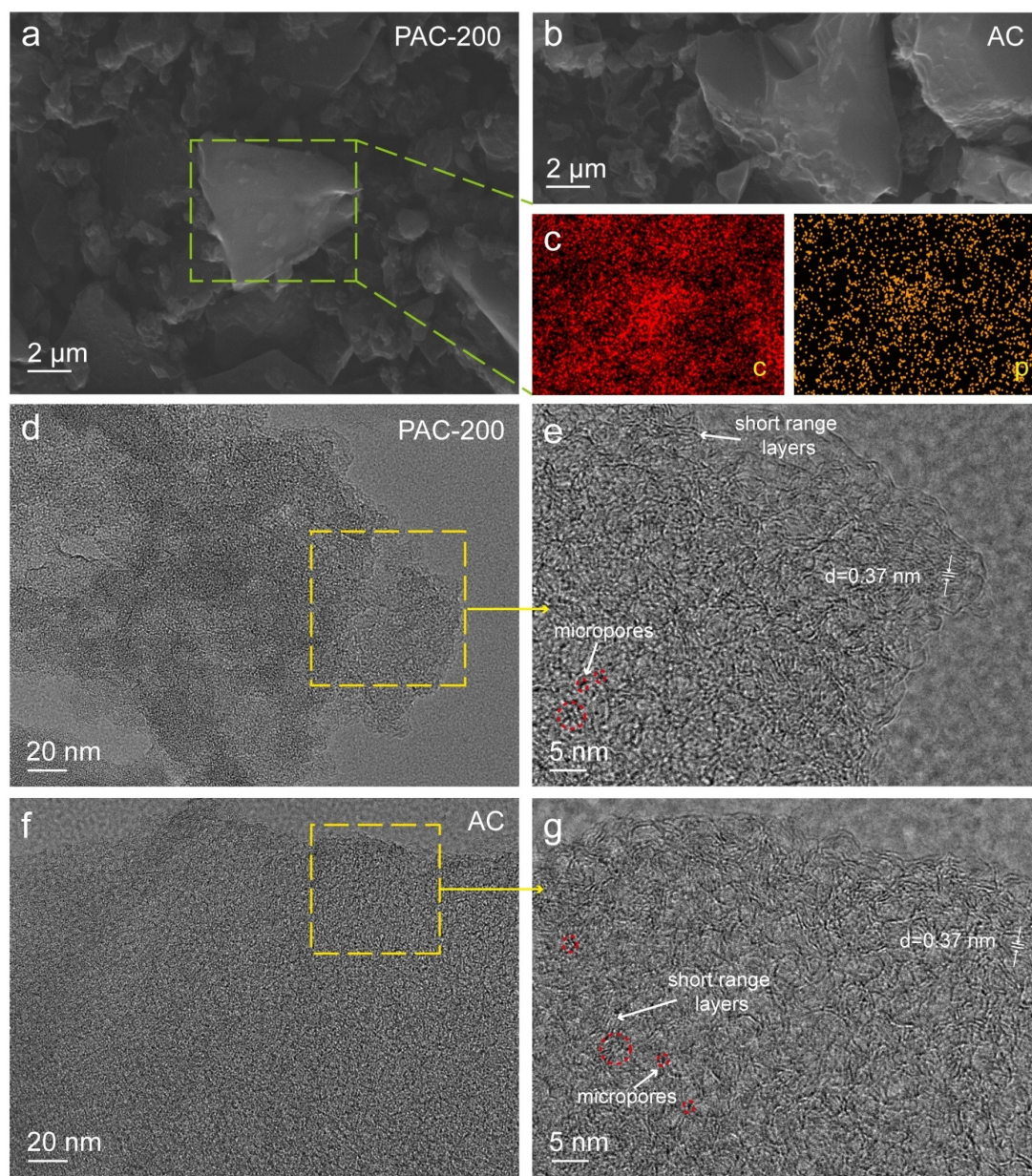
Figure 1. a) SEM image of the PAC-200 sample. b) SEM image of the AC sample. c) The EDS mapping images of the selected area highlighted in a). d) TEM image of PAC-200 sample. e) Magnified TEM image of the PAC-200 sample highlighted by the dashed box in d). f) TEM image of AC sample. g) Magnified TEM image of the AC sample highlighted by the dashed box in f). The red circles highlight the microporous structures.

and AC exhibit an extensive network of interconnected micropores, which contribute significantly to the charge storage capacity and, by extension, enhance the electrochemical performance of the electrodes in supercapacitors.[12] The SEM and TEM images collectively indicate that PAC-200 maintains a uniform and open pore structure, which facilitates deeper interlayer spacing to promote ion diffusion and shorten the ion transport pathways.

The crystal structures of AC and PAC-x (where x denotes the phosphating temperature) samples were analyzed by X-ray diffractometer (XRD) measurements. Figure S1a illustrates that both AC and PAC-x show weak and broad peaks at approximately 23° and 43°, corresponding to the (002) and (100)

planes of amorphous carbon (JCPDS card no. 75–1621). The pronounced intensity in the low-angle region ($< 15°$) for these samples suggests the presence of more microporous structures.[13] Figure 2a presents two distinct Raman peaks, located at 1338 cm^{-1} and 1583 cm^{-1}, which are attributed to the D and G bands of AC and PAC-200, respectively. The D band is the indicative of structural defects, while the G band is associated with the E_{2g} modes of graphite.[14] The intensity ratio of the D to G bands (I_D/I_G) for AC and PAC-x (x = 200, 250, 300, 350), as shown in Figure S1b, are 0.95, 0.95, 0.93, 0.92, and 0.95, respectively, indicating that phosphorus doping does not significantly alter the degree of disorder. The N$_2$ adsorption-desorption isotherms depicted in Figure 2b and
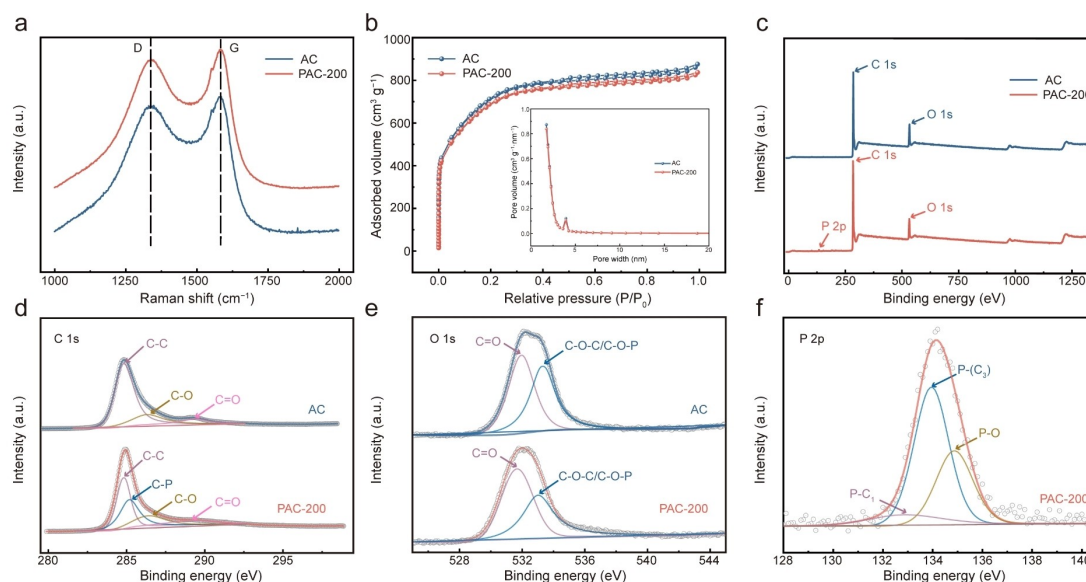
Figure 2. a) Raman spectra of the AC and PAC-200 samples. b) N$_2$ adsorption-desorption isotherms and pore size distribution of the AC and PAC-200 samples. c) The full XPS spectra of AC and PAC-200 samples. d, e) High-resolution XPS spectra of C 1s (d), and O 1s (e) for AC and PAC-200 samples. f) P 2p XPS spectrum of PAC-200 sample.
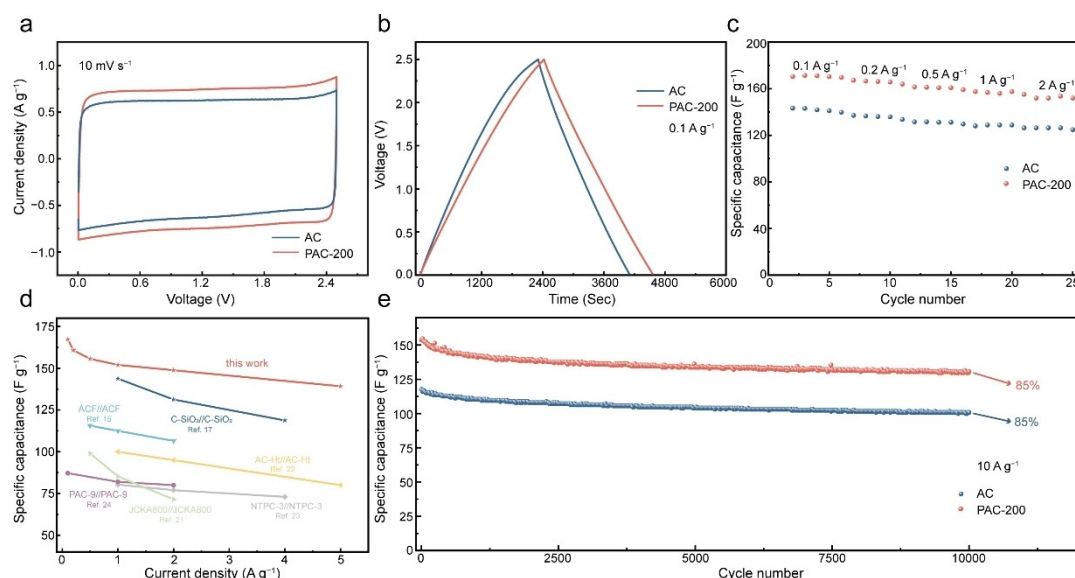
Figure S2 reveal that AC and PAC-x exhibit type I isotherms, confirming the presence of microporous structures,[15] which aligns with the XRD results. The specific surface areas of AC and PAC-X (X = 200, 250, 300, 350) electrodes are determined to be 2594.7, 2500.6, 2356.9, 2228.8, and 2249.7 m^2 g^{-1}, respectively. These data indicate a trend of decreasing specific surface area with the introduction of phosphorus doping. Moreover, the pore size distribution curves indicate that both AC and PAC-200 have a similar average pore diameter of 2.5 nm, facilitating effective adsorption and desorption of electrolyte ions such as TEA$^+$ (0.67 nm) and BF$_4^-$ (0.48 nm).[16] The predominance of micropores ensures efficient ion adsorption, which can effectively improve the charge storage capacity.

The surface chemistry of AC and PAC-200 was investigated using X-ray photoelectron spectroscopy (XPS) spectra. The full survey XPS spectra are shown in Figure 2c, in which three distinct characteristic peaks at approximately 284.4, 532.2, and 134.0 eV can be ascribed to C 1s, O 1s, and P 2p orbitals, respectively. The high-resolution C 1s core-level XPS spectrum of PAC-200 deconvolutes into four peaks positioned at 284.8, 285.2, 286.4, and 289.3 eV, corresponding to C—C, C—P, C—O, and C=O bonds, respectively (Figure 2d).[10] Notably, the intensity of the C—C peak in PAC-200 is diminished as compared to that in AC due to the emergence of the P—C peak, thereby confirming the successful incorporation of phosphorus into the carbon matrix. The O 1s core-level XPS spectrum in Figure 2e has been deconvoluted into four distinct peaks attributed to carbonyl groups (C=O) and bridge-bonded oxygen (C—O—P/ C—O—C), with binding energies of 531.6 and 533.0 eV, respectively.[17] As illustrated in Figure S3a, the full survey XPS spectra for samples PAC-250, PAC-300, and PAC-350 exhibit no significant changes. In contrast, the

intensity of bridge-bonded oxygen (C—O—P/ C—O—C) peak in the PAC samples increases progressively with the augmentation of phosphorization temperature (Figure S3b). Owing to the overlap of the C—O—C and C—O—P peaks, the changes in the C—O—P peak are not readily distinguishable. The intensity of C=O peak is more pronounced for the PAC-200 sample compared to the other PAC-x samples. The electrochemical activity of the C=O group is known to contribute significantly to the electrochemical properties of carbon materials.[18] The high-resolution P 2p core-level XPS spectrum illustrated in Figure 2f can be deconvoluted into three peaks located at 133.0, 133.9, and 134.8 eV, corresponding to the P-C$_1$, P-(C$_3$), and P—O bonds, respectively. P-(C$_3$) represents the phosphorous atoms integrated into the carbon framework and covalently bonded to the three adjacent C atoms, while P-C$_1$ denotes phosphorus atoms covalently bonded to one adjacent C atom. The introduction of P-(C$_3$) bonds creates sites with relatively weak adsorption energy. Consequently, an increase in P-(C$_3$) content enhances the expansion of the adsorption sites, thereby improving the adsorption capacity.[19] PAC-200 exhibits the highest concentration of P-(C$_3$) bonds. As shown in Figure S3c, both the P-C$_1$ and P-(C$_3$) peaks present different variations with the increasing phosphorization temperature. PAC-300, which has the lowest P-(C$_3$) content among the samples, consequently shows a relatively low specific capacitance. Additionally, phosphorus atoms substitute for carbon sites within the carbon lattice after phosphorus doping, leading to an improvement in the electrical conductivity of carbon.[20]

The AC and PAC-x electrodes are assembled into symmetrical coin-cell supercapacitors to assess their practical performance. As depicted in Figure 3a, b, the cyclic voltammetry (CV) curves recorded at a scan rate of 10 mV s^{-1} and the

Batteries & Supercaps

Research Article
doi.org/10.1002/batt.202400730

Chemistry
Europe

European Chemical
Societies Publishing

Figure 3. a) CV curves of AC//AC and PAC-200//PAC-200 symmetric coin-cell supercapacitors at 10 mV s^{-1}. b) GCD curves of AC//AC and PAC-200//PAC-200 at 0.1 A g^{-1}. c) Specific capacitances of AC//AC and PAC-200//PAC-200 at different current densities from 0.1 to 2 A g^{-1}. d) Rate capability of PAC-200//PAC-200 versus the previously published literature.[15,17,21–24] e) Cycling performance of AC//AC and PAC-200//PAC-200 at a current density of 10 A g^{-1} for 10000 cycles.

galvanostatic charge-discharge (GCD) curves measured at a current density of 0.1 A g^{-1} for both AC and PAC-200 exhibit shapes that are approximately rectangular and triangular, respectively. The CV curves display no distinct redox peaks, and the GCD curves lack reaction plateaus, which are indicative of the capacitive behavior of an ideal capacitor.[25,26] This observation suggests that the energy storage mechanism in both AC and PAC-200 is predominantly based on electric double-layer capacitance (EDLC) rather than Faradaic reactions. In addition, to elucidate the combined contributions of EDLC and pseudocapacitance in AC and PAC-200, a plot of log(I) vs. log(v) is graphed based on the CV curves at various scan rates, as illustrated in Figure S4. The relationship between peak current (I) and scan rate (v) adheres to a specific power-law,[27] as delineated in equation (4).

$$I = av^b \tag{4}$$

where I is the current density and v signifies the scan rate. The exponent b value represents the slope of the plot of log(I) vs. log(v). A b value of 0.5 indicates that diffusion-controlled process dominates, whereas a b value of 1 indicates that charge storage is primarily governed by surface capacitance.[28,29]

As illustrated in Figure S4, the b value of 0.93 for both AC and PAC-200 indicates that the charge storage kinetics are almost surface capacitance related ultrafast kinetics. Even at an elevated scan rate of 100 mV s^{-1}, the CV curves retain their well-rectangular shape, indicating the fast charge transfer within the porous electrode (Figure S5a, b). The maintenance of an approximate triangular shape at current densities ranging from 0.5 to 2 A g^{-1}, accompanied by slight *IR* drops, further confirms the excellent capacitive behavior of the PAC-200.[30] Owing to phosphorus doping, PAC-200 exhibits a superior specific capacitance of 171 F g^{-1} at 0.1 A g^{-1}, surpass-

ing to that of AC, which is 143 F g^{-1} (Figure S5c, d). Figure 3c evaluates the rate performance of the supercapacitors. PAC-200 not only demonstrates commendable rate capability across a current density range from 0.1 to 2 A g^{-1} but also displays higher specific capacitance. This enhancement is attributed to the introduction of P-(C$_3$) bonds, which endow PAC-200 with augmented active sites, thereby enhancing its electrochemical performance.

We have compared the specific capacitance of this work with that of previously reported double-layer coin-cell supercapacitors across different current densities, as depicted in Figure 3d. It is evident that the incorporation of phosphorus doping in this work has led to a marked enhancement in capacitance, augmenting the already elevated capacity levels. PAC-200 demonstrates much higher specific capacitance at all tested current densities. As shown in Figure 3e, PAC-200 yields a capacitance retention of 85% after 10,000 cycles at 10 A g^{-1}, underscoring its good cycling stability with enhanced capacitance. Figure S6 shows a comparative analysis of the electrochemical performance at varying phosphating temperatures. The interfacial resistance between the electrode and electrolyte for all samples is quantified using electrochemical impedance spectroscopy (EIS, Figure S6a). The charge transfer resistance of PAC-x samples is observed to be lower than that of AC, signifying an improved charge transfer capability due to the introduction of phosphorous. The CV, GCD, and rate performance of the PAC-200, PAC-250, PAC-300, and PAC-350 samples are detailed in Figure S6b-d. Figure S6d further reveals that PAC-200 demonstrates a superior specific capacitance of 171 F g^{-1} at a current density of 0.1 A g^{-1}, which surpasses the values observed for PAC-250 (164 F g^{-1}), PAC-300 (155 F g^{-1}), and PAC-350 (162 F g^{-1}). Consequently, the 200 °C was selected as the optimal phosphating temperature. Based on the above-mentioned results, phosphorous doping

Batteries & Supercaps

Research Article
doi.org/10.1002/batt.202400730

Chemistry Europe
European Chemical
Societies Publishing

in carbon is a double-edged sword: while the surface modification with phosphorus augments the active site count and ion adsorption capacity, excessive phosphorus modification can diminish the specific surface area. Consequently, the selection of optimal samples necessitates a delicate balance between these competing influences.

Figure 4a, b show the CV curves collected at scan rate of $10\ mV\ s^{-1}$, and corresponding electrochemical quartz crystal microbalance (EQCM) curves of AC and PAC-200 coated gold flakes in a three-electrode system containing 1 M $TEABF_4$ PC solution. The testing indicates that the electrochemical window is narrower compared to the coin cell due to the lower amount of carbon on the quartz substrate, which improves the electrochemical activity of the gold at high potentials.[31] Prior studies have documented that TEA^+ and BF_4^-, with ion sizes of 0.67 nm and 0.48 nm respectively,[16] can adsorb and desorb freely within the pores of AC and PAC-200, which possess a pore size of 2.5 nm. The EQCM curve provides a visual representation of the specific changes in adsorption quantity. The adsorption amount of PAC-200, at 5.48 µg, exceeds that of AC (1.41 µg) due to the enhanced ion adsorption by phosphorus doping.

Figure 4c, d show the change in mass (Δm) and charge (ΔQ) on the gold sheet electrode at a scan rate of $10\ mV\ s^{-1}$. The yellow dashed lines represent the theoretical mass change (Δm) of AC and PAC electrodes during polarization, plotted as a function of capacitive charge (ΔQ). The molecular weight (M_w) of species interacted with the electrode can be determined from the slope of corresponding line based on the following equation:

$$M_w = \frac{\Delta m n F}{\Delta Q} \qquad (5)$$

Δm is the electrode mass change (g). n is the valence number of the ion. F is the Faraday constant $96485\ C\ mol^{-1}$. ΔQ is the quantity of charge (C) that passes through the electrode during polarization.

The findings reveal that the charge storage mechanism of AC within the potential window of 0 to 1.2 V can be elucidated as follows: At low charge densities, the slope of the plot deviates from the theoretical line representing the desorption of bare cations (yellow dashed line), suggesting that the transfer of TEA^+ cations is not the exclusive process during charging. Instead, an ion exchange process is involved, where anions are preferentially adsorbed and cations are correspondingly desorbed. The high relative molecular mass of the cations results in a reduction of total mass. Conversely, at high charge densities, the slope of the plot aligns with the theoretical line (yellow dashed line) that corresponds to the exclusive adsorption of bare anions. It is suggesting that counter-ion adsorption becomes predominant, leading to an increase in total mass (Figure 4c).[32] Following phosphorus doping, the charge storage mechanism of PAC-200 undergoes significant changes, with ion exchange emerging as the predominant mechanism across the full potential range of 1.2 V (Figure 4d). This phenomenon occurs because PAC-200 absorbs a greater number of cations, which facilitates the initial adsorption of additional cations at the electrode surface before charging. This enrichment of cations allows more cations to be desorbed during charging, thus remaining an ion exchange mechanism throughout the charging process. The ion exchange mechanism is advantageous as it offers a larger capacitance as compared to traditional counter ion adsorption.[33–35] From a thermodynamic perspective, during the charge-discharge cycle, the charge storage mechanism that minimizes the variation in free energy, specifically the
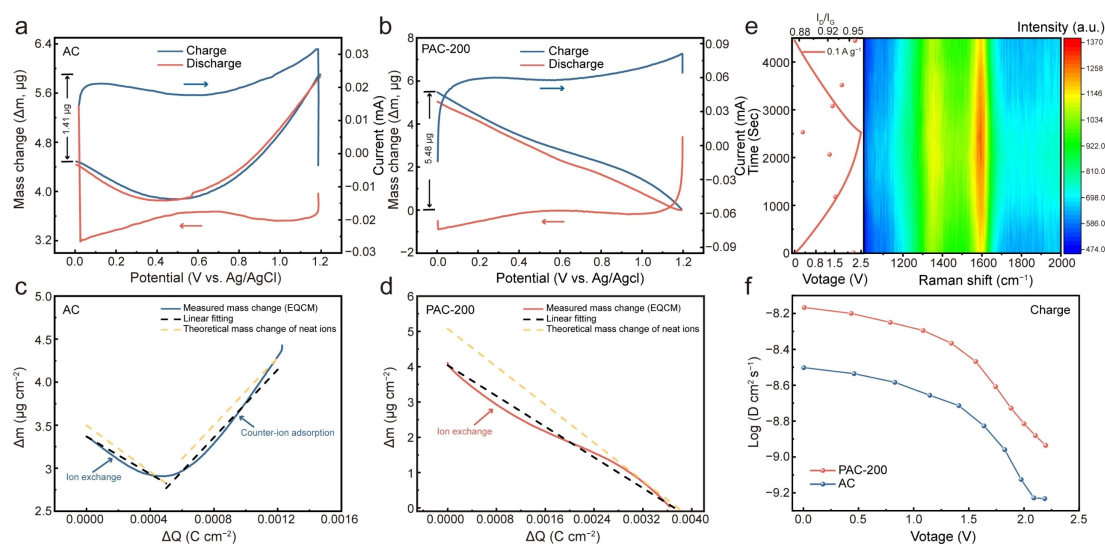

Figure 4. a, b) CV curves and mass changes of AC and PAC-200 in the three-electrode system using 1 M $TEABF_4$/PC solution. c) The variation in electrode mass relative to charge (denoted by blue solid line) during the positive polarization of AC. d) The variation in electrode mass relative to charge (denoted by red solid line) during the positive polarization of PAC-200. The yellow dashed lines represent the theoretical mass changes for pure ions, as determined by calculations based on Faraday's laws. The black dashed line delineates the linear fitted to the experimental mass change data. e) In situ Raman spectra and corresponding GCD curve of PAC-200 at 0.1 A g^{-1}. f) Diffusion coefficients of AC and PAC-200 calculated from the galvanostatic intermittent titration technique (GITT) profiles during the charging process.

Batteries & Supercaps

Research Article
doi.org/10.1002/batt.202400730

Chemistry Europe
European Chemical
Societies Publishing

voltage change per unit charge, is conducive to achieving high capacitance.[34] In the context of counter-ion adsorption process, when an ion is entering a pore, there will be an entropic penalty to increase the free energy.[35] Moreover, the packing of the ions inside the pores engenders an unfavorable enthalpic penalty. In contrast, within the ion exchange mechanism, the total in-pore ion density remains constant throughout the charging process, thereby mitigating the enthalpic penalty associated with denser ion packing. Concurrently, the corresponding entropic penalty is also diminished. Therefore, the ion exchange mechanism incurs a reduced thermodynamic cost during charging, which contributes to the observed enhancement in specific capacitance. Noted that activated carbon electrodes usually exhibit distinct charge storage mechanisms under positive and negative polarization.[32,36,37] We thus have conducted EQCM measurements for PAC-200 under negative polarization to provide a comprehensive analysis of its charge storage behavior. As illustrated in Figure S7, the slope of the linear fit of the experimental mass change versus charge, in accordance with Faraday's law, yields an experimental molar mass of 268 g mol^{-1} per adsorbed species, which exceeds the theoretical molar mass of pure TEA^+ (130 g mol^{-1}). The higher experimental molar mass compared to the theoretical value suggests that the charge storage mechanism for PAC-200 during negative polarization involves counter-ion adsorption, specifically with TEA^+ as the counter ion. The additional molar mass of 138 g mol^{-1} can be attributed to the co-adsorption of solvent molecules.[36]

The in situ Raman spectroscopic characterization of PAC-200, as depicted in Figure 4e, reveals obvious changes during the charging process up to 2.5 V. The intensities of both the D band and G band are observed to increase, while concurrently, the I_D/I_G ratio demonstrates a continuous decrease. This trend suggests a reduction in disorder within the material, implying an improvement in the structural order as the material undergoes charging.[38] Upon discharging to 0 V, the I_D/I_G ratio nearly revert to the initial value, indicating that the PAC-200 has excellent structural stability and good reversibility.[39] The kinetics is further evaluated by determining the diffusion coefficient of TEA^+ (D_{TEA^+}) in porous structures through GITT measurements, which involve a 4-minute charging period at 0.1 A g^{-1} followed by a 4-minute relaxation. The results are depicted in Figure 4f and Figure S8a. PAC-200 clearly achieves a much higher diffusion coefficient compared to AC, suggesting that phosphorus doping improves the ion transport kinetics within the porous structure. As illustrated in Figure S8b, the PAC-200 exhibits a lower self-discharge rate.[40] Due to the inhomogeneous pore structure, self-discharge is an inevitable phenomenon that typically results from charge redistribution.[41,42] Phosphorus, with its strong electronegative group, increases the ion adsorption onto the electrode surface, which inhibits the ion redistribution process and subsequently reduces the self-discharge rate.

A symmetrical pouch cell supercapacitor was assembled to underscore the commercialization viability of PAC-200, as depicted in Figure 5a. Figure 5b illustrates that the ideal triangular shape is maintained at current densities ranging from 0.1 A g^{-1} to 2 A g^{-1} without significant IR drop, indicating good capacitive behavior. The rate capability of the pouch cell is exemplified in Figure 5c. The PAC-200 yields a specific capacitance of 166 F g^{-1} at a current density of 0.1 A g^{-1}. When the current density is elevated to 2 A g^{-1}, the specific capacitance of PAC-200 is robustly maintained at 148 F g^{-1}. The Ragone plot, which delineates the relationship between energy density and power density, is presented in Figure 5d. The symmetrical pouch cell achieves a noteworthy energy density of 36.2 Wh kg^{-1} at a power density of 113.9 W kg^{-1} and
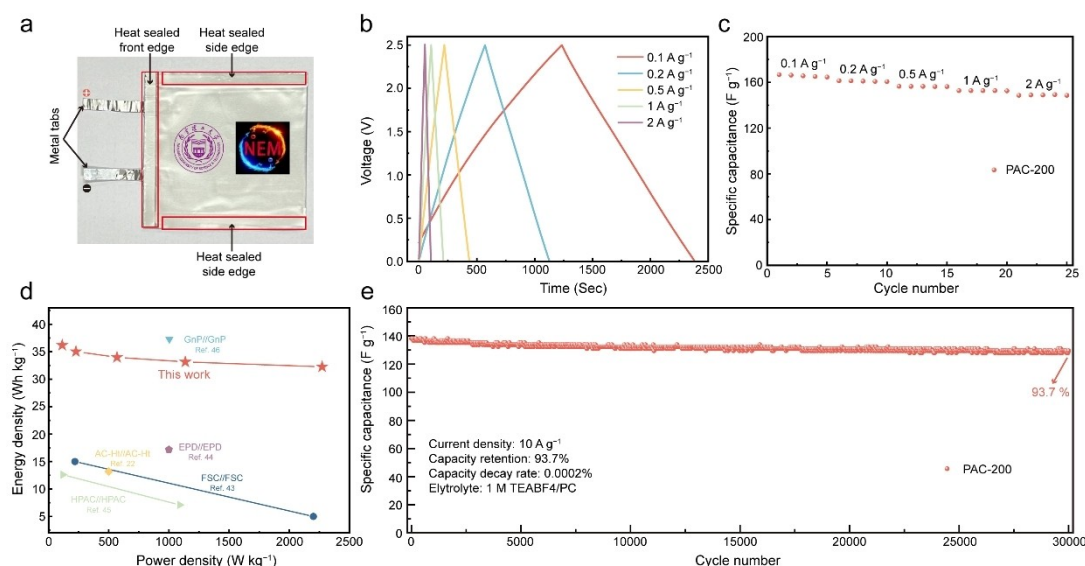
Figure 5. PAC-200 based symmetric pouch cell supercapacitor in the voltage window 0–2.5 V. a) Configuration of the pouch cell. b) GCD curves at different current densities ranging from 0.1 to 2 A g^{-1}. c) Specific capacitances at different current densities. d) Ragone plot of as-assembled pouch cell. Previously reported values of carbon-based supercapacitors were added for comparison.[22,43–46] e) Long cycling performance for 30000 charge-discharge cycles at a current density of 10 A g^{-1}.

Batteries & Supercaps

Research Article
doi.org/10.1002/batt.202400730

Chemistry Europe
European Chemical
Societies Publishing

it maintains 32.3 Wh kg^{-1} at an increased power density of 2272.8 W kg^{-1}. These metrics surpass those reported in the literature for carbon-based pouch supercapacitors. In addition, as shown in Figure 5e, the pouch cell exhibits a capacitance retention of 93.7% after 30,000 cycles at a current density of 10 A g^{-1}, thereby attesting to the durability and enduring high performance of the symmetrical device under long-term operational conditions.

3. Conclusions

In summary, the phosphorus doping of AC successfully incorporates P-(C$_3$) into the carbon structure. This treatment results in enhanced conductivity and reduced charge transfer resistance in PAC-200. The as-assembled PAC-200//PAC-200 symmetric coin-cell supercapacitors demonstrate a superior specific capacitance of 171 F g^{-1} at 0.1 A g^{-1}, outperforming both untreated AC (143 F g^{-1} at 0.1 A g^{-1}) and commercial activated carbon (YP50F, 96 F g^{-1} at 0.5 A g^{-1}). Moreover, the symmetrical pouch cell supercapacitor achieves a high energy density of 36.2 Wh kg^{-1} at a power density of 113.9 W kg^{-1}, and it retains 93.7% of its capacitance after 30,000 cycles. Our findings indicate that phosphorus doping intensifies adsorption capabilities, thereby facilitating the initial adsorption of additional cations onto the electrode prior to the charging process. This enrichment of cations enables a greater number to be desorbed during charging, maintaining an ion exchange mechanism throughout the charging process. Consequently, it provides a larger specific capacitance when cations are the primary charge carriers. This insight deepens our understanding of the adsorption/desorption dynamics in phosphorus-doped porous carbon materials, which is essential for the development of next-generation supercapacitors with high energy density.

Conflict of Interests

The authors declare no conflict of interest.

Data Availability Statement

The data that support the findings of this study are available on request from the corresponding author. The data are not publicly available due to privacy or ethical restrictions.

[1] Y. Chen, G. Xie, R. Sun, X. Gao, Z. Pan, B. Cui, X. Gong, C. Yang, *Mater. Today Commun.* **2024**, *39*, 108814.
[2] J. Guo, D. Wu, T. Wang, Y. Ma, *Appl. Surf. Sci.* **2019**, *475*, 56–66.
[3] G. Zhang, T. Guan, N. Wang, J. Wu, J. Wang, J. Qiao, K. Li, *Chem. Eng. J.* **2020**, *399*, 125818.
[4] X. Yin, J. Zhang, L. Yang, W. Xiao, L. Zhou, Y. Tang, W. Yang, *Sci. China Mater.* **2021**, *65*, 383–390.
[5] W. Ma, L. Xie, L. Dai, G. Sun, J. Chen, F. Su, Y. Cao, H. Lei, Q. Kong, C.-M. Chen, *Electrochim. Acta* **2018**, *266*, 420–430.
[6] D. Salinas-Torres, S. Shiraishi, E. Morallón, D. Cazorla-Amorós, *Carbon* **2015**, *82*, 205–213.
[7] Y. Zheng, K. Chen, K. Jiang, F. Zhang, G. Zhu, H. Xu, *J. Energy Storage* **2022**, *56*, 105995.
[8] L. Xu, W. Guo, L. Zeng, X. Xia, Y. Wang, P. Xiong, Q. Chen, J. Zhang, M. Wei, Q. Qian, *Chem. Eng. J.* **2021**, *419*, 129607.
[9] X. Ma, N. Xiao, J. Xiao, X. Song, H. Guo, Y. Wang, S. Zhao, Y. Zhong, J. Qiu, *Carbon* **2021**, *179*, 33–41.
[10] G. Zhong, S. Lei, X. Hu, Y. Ji, Y. Liu, J. Yuan, J. Li, H. Zhan, Z. Wen, *ACS Appl. Mater. Interfaces* **2021**, *13*, 29511–29521.
[11] Z. Liu, H. Peng, X. Xie, X. Wang, Y. Pu, G. Ma, Z. Lei, *J. Power Sources* **2022**, *543*, 231831.
[12] C. Zhang, H. Du, K. Ma, Z. Yuan, *Adv. Energy Mater.* **2020**, *10*, 2002132.
[13] X. Zhang, Y. Wang, X. Yu, J. Tu, D. Ruan, Z. Qiao, *J. Energy Storage* **2021**, *44*, 103378.
[14] S. S. Gunasekaran, S. Badhulika, *Energy Storage* **2022**, *5*, e404.
[15] M. Vijayakumar, R. Santhosh, J. Adduru, T. N. Rao, M. Karthik, *Carbon* **2018**, *140*, 465–476.
[16] J. Zhang, H. Yang, Z. Huang, H. Zhang, X. Lu, J. Yan, K. Cen, Z. Bo, *Waste Disposa Sustainable Energy* **2023**, *5*, 417–426.
[17] B. Liu, X. Wang, Y. Chen, H. Xie, X. Zhao, A. B. Nassr, Y. Li, *J. Energy Storage* **2023**, *68*, 107826.
[18] W. Yang, W. Yang, L. Kong, A. Song, X. Qin, G. Shao, *Carbon* **2018**, *127*, 557–567.
[19] J. Yan, H. Li, K. Wang, Q. Jin, C. Lai, R. Wang, S. Cao, J. Han, Z. Zhang, J. Su, K. Jiang, *Adv. Energy Mater.* **2021**, *11*, 2003911.
[20] J. Gong, G. Zhao, J. Feng, G. An, T. Li, L. Zhang, B. Li, Z. Qian, *ACS Nano* **2020**, *14*, 14057–14069.
[21] M. Bora, J. Tamuly, S. Maria Benoy, S. Hazarika, D. Bhattacharjya, B. K. Saikia, *Fuel* **2022**, *329*, 125385.
[22] I. I. Gurten Inal, Z. Aktas, *Appl. Surf. Sci.* **2020**, *514*, 145895.
[23] Y. Zhang, H. Fang, L. Guan, Y. Li, Y. Yao, Y. Wan, D. Kong, M. Huang, W. Wang, B. Wang, N. Wang, D. Zhang, Y. Li, M. Wu, *J. Power Sources* **2024**, *593*, 233966.
[24] J.-H. Kim, Y.-J. Kim, S.-C. Kang, H.-M. Lee, B.-J. Kim, *Minerals* **2023**, *13*, 802.
[25] F. Chi, C. Li, Q. Zhou, M. Zhang, J. Chen, X. Yu, G. Shi, *Adv. Energy Mater.* **2017**, *7*, 1700591.
[26] Y. Yusran, H. Li, X. Guan, D. Li, L. Tang, M. Xue, Z. Zhuang, Y. Yan, V. Valtchev, S. Qiu, Q. Fang, *Adv. Mater.* **2020**, *32*, e1907289.
[27] T. Islam, M. M. Hasan, S. S. Shah, M. R. Karim, F. S. Al-Mubaddel, M. H. Zahir, M. A. Dar, M. D. Hossain, M. A. Aziz, A. J. S. Ahammad, *J. Energy Storage* **2020**, *32*, 101908.
[28] Y. Sun, D. Xu, S. Wang, *Carbon* **2022**, *199*, 258–267.
[29] V. S. Bhat, A. Toghan, G. Hegde, R. S. Varma, *J. Energy Storage* **2022**, *52*, 104776.
[30] G. Li, Y. Ji, D. Zuo, J. Xu, H. Zhang, *Adv. Compos. Hybrid Mater.* **2019**, *2*, 456–461.
[31] W. Y. Tsai, P. L. Taberna, P. Simon, *J. Am. Chem. Soc.* **2014**, *136*, 8722–8728.
[32] M. D. Levi, N. Levy, S. Sigalov, G. Salitra, D. Aurbach, J. Maier, *J. Am. Chem. Soc.* **2010**, *132*, 13220–13222.
[33] S. Bi, X. Knijff, X. Lian, A. van Hees, C. Zhang, M. Salanne, *ACS Nano* **2024**, *18*, 19931–19949.
[34] A. C. Forse, C. Merlet, J. M. Griffin, C. P. Grey, *J. Am. Chem. Soc.* **2016**, *138*, 5731–5744.
[35] S. Kondrat, A. A. Kornyshev, *Nanoscale Horiz.* **2016**, *1*, 45–52.
[36] J. M. Griffin, A. C. Forse, W. Y. Tsai, P. L. Taberna, P. Simon, C. P. Grey, *Nat. Mater.* **2015**, *14*, 812–819.
[37] L. Niu, L. Yang, J. Yang, M. Chen, L. Zeng, P. Duan, T. Wu, E. Pameté, V. Presser, G. Feng, *Ind. Chem. Mater.* **2023**, *1*, 175–187.

[38] R. Venâncio, R. Vicentini, L. H. Costa, R. Teófilo, L. M. Da Silva, H. Zanin, *J. Energy Storage* **2022**, *50*, 104219.

[39] C. Lu, Z. Sun, L. Yu, X. Lian, Y. Yi, J. Li, Z. Liu, S. Dou, J. Sun, *Adv. Energy Mater.* **2020**, *10*, 2001161.

[40] X. Su, W. Jia, H. Ji, Y. Zhu, *J. Energy Storage* **2021**, *41*, 102830.

[41] Y. M. Volfkovich, A. Y. Rychagov, A. A. Mikhalin, V. E. Sosenkin, E. N. Kabachkov, Y. M. Shulga, A. Michtchenko, *J. Electroanal. Chem.* **2022**, *910*, 116198.

[42] R. Yuan, Y. Dong, R. Hou, S. Zhang, H. Song, *J. Electrochem. Soc.* **2022**, *169*, 030504.

[43] P. A. Zingare, S. J. Dhoble, A. D. Deshmukh, *Diamond Relat. Mater.* **2022**, *124*, 108925.

[44] B. K. Chakrabarti, K. B. Dönmez, Z. Çobandede, C. T. J. Low, *ChemElectroChem* **2024**, *11*, e202400244.

[45] T. F. Hung, T. H. Hsieh, F. S. Tseng, L. Y. Wang, C. C. Yang, C. C. Yang, *Nanomaterials* **2021**, *11*, 785.

[46] T. Cetinkaya, R. A. W. Dryfe, *J. Power Sources* **2018**, *408*, 91–104.